RSC Advances

ROYAL SOCIETY OF CHEMISTRY

www.rsc.org/advances

A simple growth method for Nb_2O_5 films and their optical properties

J. K. Dash, [a,*] L. Chen, [a] Michael R. Topka, [b] Peter H. Dinolfo, [b] L.H. Zhang, [c] K. Kisslinger, [c] T.–M. Lu [a] and G.–C. Wang [a]

Abstract

A simple method for the synthesis of Nb_2O_5 films of thicknesses ranging from tens to several hundreds of nanometers on amorphous silicon dioxide or quartz substrates is presented. Nb_2O_5 films were formed by annealing the sputter deposited Nb films under Ar flow and without oxygen plasma in a quartz tube within a furnace at 850 ^oC. The structural, compositional, optical, and vibrational properties were characterized by grazing incidence X-ray diffraction, transmission electron microscopy, X-ray photoelectron spectroscopy, ultraviolet visible spectroscopy, and Raman scattering. Each of the Nb_2O_5 films is polycrystalline with an orthorhombic crystal structure. We observed vibrational modes including longitudinal optical, transverse optical, and triply degenerate modes, and measured the indirect optical band gap to be ~ 3.65 eV. The transmittance spectrum of the ~ 20 nm thick Nb_2O_5 film shows over 90 % transmittance below the band gap energy in the visible wavelength range and decreases to less than 20 % in the ultraviolet regime. The optical properties of the films in the UV-Vis range show potential applications as UV detectors.

1. Introduction

Niobium oxides have attracted attention among researchers for their rich charge states, phases, morphologies, and associated properties. The number of charge states of niobium ranges from +2 to +4 to +5 for NbO, NbO_2 and Nb_2O_5, respectively. These suboxides can be a conductor, an n-type

semiconductor, or an insulator. Nb_2O_5 has the highest heat of formation (-1899.54 ± 8.37 kJ/mol) compared with NbO_2 (-792.87 ± 6.28 kJ/mol) and NbO (-407.94 ± 12.55 kJ/mol) [1] and is the most stable once it is formed. The Nb_2O_5 exists in various phases including pseudohexagonal (TT-phase), orthorhombic (T-phase), and monoclinic (H-phase). Various physical or chemical processing methods have been developed to prepare Nb_2O_5 thin films and nanostructures. Examples of Nb_2O_5 thin film preparations are reactive sputtering of a Nb target in an Ar-O_2 plasma on SiO_2/Si substrates [2, 3] or in an atmosphere composed of oxygen and argon, [4] pulsed laser deposition of Nb on Si followed by exposure to atmosphere, [5] reactive RF magnetron sputtering of a Nb_2O_5 target on glass substrates, [6] atomic layer deposition, [7] and sol-gel dip coating. [8] The extended sol-gel method was also used to form nanocrystalline Nb_2O_5 films. [9] Other nanostructures synthesized by chemical processes in the form of nanowires, [10-12] nanorods, [13-15] nanotubes, [16-18] nanobelts, [19, 20] nanopores, [21] nanopowders, [22] and nanohollow fibers [23] have been reported. A wide range of potential applications has been demonstrated: catalysis, [24] gas sensors, [12, 21] electrochromic windows, [25] photodetectors, [19] electron field emitters, [11] and solid oxide fuel cells. [26]

In this work we report a simple method to fabricate ultrathin Nb_2O_5 films by post annealing the magnetron sputtered Nb films. We study their properties including structure, chemical composition, optical transmittance and reflection, optical bandgap, surface morphology, and vibrational modes. The characterization techniques used are grazing incidence X-ray diffraction (GIXRD), transmission electron microscopy (TEM), X-ray photoelectron spectroscopy (XPS), ultraviolet visible (UV-VIS) spectroscopy, atomic force microscopy (AFM), X-ray specular reflectivity (XRR), and Raman scattering.

The advantages of our ultrathin Nb_2O_5 film growth method are (1) the oxide film thickness can be controlled by the initial thickness of the Nb film and the oxide film is continuous, (2) there is no need to

use the oxygen plasma, pulsed laser, or chemical precursors, but it only needs an Ar flow in the quartz tube in a furnace, and (3) the optical properties including transmittance, reflection and optical bandgap energy of 3.65 eV are suitable for UV detection.

2. Experimental

Ultrathin Nb films of thicknesses 5, 10, 100, and 300 nm were deposited by DC magnetron sputter deposition on 300 nm thick SiO_2 covered Si(001) substrates (of resistivity 0.001-0.005 ohm cm) and quartz slides (Structure Probe, Inc.). The base pressure of the sputter deposition chamber was ~ 7.5×10^{-7} Torr. The Ar gas flow rate was controlled at 2.01 Standard Cubic Centimeters per Minute (sccm) and the working pressure of Ar was set to 2.3 mTorr. The power was set to 50 W. The Nb target (99.95% purity) was a 3-inch round disk and the distance from the target surface to the center of the substrate was ~15 cm. The deposition rate was ~ 3.5 nm/min. This deposition rate was calibrated from the cross sectional image obtained from the scanning electron microscopy (SEM).

The Nb ultrathin films on SiO_2/Si and quartz substrates were then placed in a quartz boat (100 × 45 × 20 mm) positioned at the center of a 30-inch long quartz tube with outside and inside diameters of 59 and 55 mm, respectively. This quartz tube was placed inside a one zone furnace and then purged with an ultrahigh purity Ar gas (99.999 %) at a flow rate of 950 sccm. After 20 min of Ar purging, the Ar flow rate was reduced to 200 sccm while the quartz boat was gradually heated up from room temperature to 850 ^{o}C in the furnace over about 80 min. The temperature was measured using a type K thermocouple with an accuracy of ± 5 ^{o}C. The boats were kept at 850 °C for 30 min before the furnace filament current was reduced to zero over 5 - 6 min. The quartz tube then cooled down to room temperature in about 120 min. Ar gas purging was continuous during the entire heating up and cooling down processes. The temperature ramping was managed using a Eurotherm 2116 PID programmable

temperature controller attached to the furnace. The furnace and Ar gas handling lines were placed inside a venting hood. Figure 1(a) shows a schematic of the sputter deposited Nb film on SiO_2/Si. For optical measurements the Nb films were sputter deposited on quartz substrates. Fig. 1(b) shows a TEM cross-sectional view of a Nb_2O_5 film synthesized from a 300 nm thick Nb film grown on a SiO_2/Si(001) substrate that was annealed at 850 °C for 30 min inside the quartz tube furnace. The uniform contrast areas near the bottom left are Si and SiO_2. The area to the right of SiO_2 is the Nb_2O_5 film followed by a thin layer of epoxy (M-bond) and a Pt layer. The 300 ± 5 nm thickness of the SiO_2 layer is in agreement with the vender's thickness specification. The thickness of the Nb_2O_5 film is 800 ± 20 nm. This oxide layer is a result of the oxidation of the 300 nm thick Nb film. Many grains with sizes on the order of hundreds nm to microns are seen.

Grazing incidence X-ray diffraction (GIXRD) theta-2theta (θ-2θ) scans were collected using a PANalytical X'Pert Pro diffractometer to characterize the atomic structure and average grain size of the Nb_2O_5 films. A parallel X-ray beam generated from a parabolic mirror with a wavelength of 1.5405 Å was incident on the sample at a fixed 1.5° grazing angle (ω). A point detector with a 0.013° scanning step size and a 0.25 s counting time at each step, was used to collect X-ray diffraction scans. During the GIXRD scan, the ω was fixed at 1.5° while the 2θ was varied. The detector scanned over 2θ in the scattering plane while the source and sample stage were fixed. The detector was scanned in the scattering plane that contains the incident X-ray and the surface normal.

For the TEM sample, a thin layer of epoxy (M-bond) was applied to the surface of the Nb_2O_5 film. A sacrificial Pt layer was deposited on the surface of the epoxy layer for focused ion beam (FIB)/scanning electron microscopy (SEM) sample preparation. The sample was then thinned by FIB milling using energetic gallium ions. The thinned sample was mounted on a liquid nitrogen cooled sample stage to minimize the sample's mechanical drifting. A 200 keV energy electron beam was used to obtain the TEM (JEOL 2100 F) bright field images, high resolution images, and electron diffraction patterns.

X-ray photoelectron spectroscopy (XPS) was used to determine the near surface composition. The nearly monochromatic X-ray Mg K-alpha source (PHI model 04-151) had a primary energy of 1253.6 eV. The X-ray source was operated at 270 W with a 10 kV high-voltage bias and an emission current of 27 mA. A double pass cylindrical mirror energy analyzer (PHI model 15-255G) in a high vacuum chamber was used to detect the emitted electrons from the sample surface. A high-resolution spectrum was averaged from 40 repeated scans at a passing energy of 50 eV. The energy resolution of the analyzer at this passing energy is about 0.7 eV. The energy step size (0.08 eV) used to scan Nb and O peaks is smaller than 0.7 eV in order to provide a good relative resolution, defined as $R = \Delta E/E_o$, where ΔE is the passing energy and E_o is the kinetic energy of a peak position. [27]

UV-visible reflectance and transmission spectra were collected to determine the optical band gap of the ultrathin Nb_2O_5 films on quartz. The spectra were obtained from a Perkin-Elmer Lambda 950 UV/VIS Spectrometer. The transmission spectra were obtained with the slides held normal to the incident light beam in air and were corrected for the quartz background. Specular reflectance spectra were obtained at a near-normal incidence angle of 6°.

The AFM surface morphology images were collected using a PSI XE100 in non-contact mode. The HI'RES-C14/CR-AU AFM tip used has a tip radius of ~ 1 nm, a force constant of 5 N/m and a resonant frequency of 160 kHz.

X-ray reflectivity (XRR) scan obtained for the Nb_2O_5 films grown on quartz were used to determine thickness, surface roughness and density. XRR scans were taken with a Bruker D8 Discover X-ray Diffractometer using a 2-circle $\theta/2\theta$ goniometer, a centric Eulerian cradle, and a sealed copper tube X-

ray source (Cu κ_α, λ = 1.54 Å) operated at 40 kV. A 40 mm Gobel collimating mirror and a four-position rotary absorber were used for the incident beam with attenuations of approximately 1:1, 1:10, 1:100 and 1:1000. Slits of 1.0 mm and 0.2 mm were used before and after the rotary absorber, respectively. A knife edge was employed to optimize the measurements. Data were collected at grazing incidence angles ranging from 0 to 5˚ at 0.01˚ increments and repeated scans were collected and averaged until the desired signal to noise level was reached.

Raman spectra that provide vibrational mode information were collected using a Witec Alpha 300 confocal Raman microscope. The laser wavelength and power used for the measurements of the Raman spectra were 532.1 nm and 17 mW, respectively. A 100× objective lens produced a spot size of ~ 721 nm (= 1.22 × wavelength/numerical aperture of 0.9 for the 100× objective lens). The spectral resolution and step size used in Raman scattering data collection were each 0.02 cm^{-1}.

3. Results

3. 1. Structural property

3.1.1. Grazing incidence X-ray diffraction

Figure 2 shows GIXRD θ-2θ scans of the 300 nm thick SiO_2/Si(001) substrate, 5 nm thick Nb on SiO_2/Si(001), and the synthesized Nb_2O_5 films from 5, 10, 100, and 300 nm thick Nb on SiO_2/Si(001). The intensity from SiO_2/Si(001) is mostly flat over the 2θ range with the exception of a low intensity bump near 22.8^o that is from reported short range (~ 1 nm) order in SiO_2 measured by X-ray diffraction. [28, 29] For the 5 nm Nb, film there is a peak at 38.6^o from the (110) planes of Nb. See Table 1 for Bragg peak positions. The Nb film has a bcc structure and the (110) is the lowest surface energy plane. According to the structure zone model, [30, 31] the surface atoms' mobility is high in zone II and atoms form the lowest surface energy (110) plane parallel to the surface. (Note that our GIXRD-

measured plane corresponding to the (110) peak is not exactly parallel to the surface. ~17.8° from the substrate normal = theta angle of 19.3° - X-ray grazing incident angle of 1.5°). For the film synthesized from the 5 nm thick Nb film, the (110) peak disappears but two new peaks appear at $2\theta = 22.6^{o}$ and 46.1^{o}. These are identified as (001) and (002) reflections of Nb_2O_5 using lattice constant c = 3.930 Å. Similar to the film synthesized from the 5 nm thick Nb film, a GIXRD scan from the film synthesized from the 10 nm thick Nb film has (001) and (002) peaks with slightly higher intensities. For the films synthesized from the 100 nm and 300 nm Nb films, two additional peaks appear at 28.4^{o} and 36.6^{o}. When the GIXRD 2θ scan range is greater than 50^{o}, two peaks at 50.9^{o} and 55.1^{o} are also observed. These four additional peak positions are in agreement with the calculated peak positions of the (180), (181), (380) and (182) planes using the lattice constants a = 6.175 Å, b = 29.175 Å and c = 3.930 Å, and angles $\alpha = \beta = \gamma = 90^{o}$. The above results show that the films synthesized from all thickness of Nb films have a Nb_2O_5 orthorhombic phase with a Pbam space group. [32] The [001] direction has a lattice constant c. For the films synthesized from the 100 nm and 300 nm thick Nb films there are more orientations than just (001). These additional Nb_2O_5 orientations are (180), (181), (380), and (182). For the film synthesized from the 300 nm thick Nb film there is a small (110) peak at 38.58^{o}.

From the full-width-at-half-maximum (FWHM) of a peak intensity profile one can estimate the average ordered crystallite size using the Scherrer formula. That is, the average crystallite size = $k\lambda/(\beta\cos\theta)$, where k is a shape factor of about 0.9, λ is the wavelength of the X-ray, β is the FWHM in radians, and θ is the Bragg angle in degrees. Note that the size obtained from the Scherrer formula is smaller than or equal to the actual grain size. This is because there are lattice imperfections such as stacking faults and dislocations that can contribute to the peak broadening in addition to the finite crystallite size. Also, there is a small broadening due to instrument effects. From the FWHM of the (110) peak, the average crystallite size of the thinnest pure Nb film is estimated to be 5.5 nm. This is consistent with the

intended 5 nm thick sputtered Nb film. The average crystallite sizes of the Nb_2O_5 films estimated from the (001) peaks of the synthesized films from 5, 10, 100, and 300 nm thick Nb films are about 12.5 ± 0.2, 18.6 ± 0.2, 30.8 ± 0.4, and 42.6 ± 0.4 nm, respectively. The crystallite size increases as the starting Nb film thickness increases. The increased crystallite sizes of the Nb_2O_5 films relative to the original smooth Nb films (see Figs. 6(a) and 6(b) later) result from the synthesized Nb_2O_5 films having a 3D island structure with a height distribution (see Figs. 6(c) and 6(d) later), rather than being smooth and continuous films. The crystallite size extracted from the small (110) peak of Nb from the Nb_2O_5 film synthesized from the 300 nm thick Nb film is about 14.8 ± 0.2 nm.

3.1.2 High resolution TEM image and diffraction pattern

Figures 3(a) and 3(b) show a high resolution TEM image of the 800 ± 20 nm thick Nb_2O_5 film and a selected area TEM diffraction pattern (DP) of the same film, respectively. The zone axis is along the [100], or **a** direction. Line scans in Fig. 3(a) show the spacing between adjacent atoms along the [001], or **c** direction is uniform with average measured spacing of c = 0.390 ± 0.010 nm. However, the spacing among the adjacent atoms in the [010], or **b** direction is not as uniform. First, the atoms are not all aligned in a straight line along the **b** direction; some deviate from the straight line. Secondly, the spacing between two adjacent atoms also varies. This is consistent with the spacing variation of atomic positions, as determined from X-ray diffraction. [32] The lattice spacing along the **b** direction determined from X-ray peak positions such as (180) and (181) discussed in section 3.1.1 is 2.9175 nm. We have measured the repeated equivalent spacing (unit length) over hundreds of nm along the **b** direction using ImageJ software to analyze the high resolution TEM image and have obtained an average spacing of 2.83 ± 0.05 nm labeled as b between the two arrows shown in Fig. 3(a). To determine the unit length along the **b** direction more accurately we use the diffraction pattern shown in Fig. 3(b) next.

The lengths of the reciprocal unit vectors **c*** and **b*** are measured from the spots in the DP shown in Fig. 3(b). We measured the reciprocal length b* between the 2nd order spots in the positive and negative **b*** directions, or 4b*, and then divided by 4. (The 000 spot is too strong and the TEM beam stopper blocks the spot.) The measured values are c*= 2.64 ± 0.01 nm^{-1} and b*= 0.357 ± 0.005 nm^{-1}. The inverses of c* and b* correspond to real space spacings c ≈ 0.378 nm and b ≈ 2.80 nm, respectively. These are in reasonable agreement with the measured real space unit lengths c and b shown in Fig. 3(a) as well lattice constants obtained from X-ray diffraction. Miller indices of the stronger diffraction spots are labeled. All reciprocal lattice vector lengths G(*hkl*) match well to the real space spacings d_{hkl} through d_{hkl} = 1/G(*hkl*). The fast Fourier transform of the real space image shown in Fig. 3(a) using ImageJ software [33] gives a DP in agreement with the observed DP. The real space high resolution image in Fig. 3(a) shows that many stacking faults exist along the **b** direction. The stacking faults give raise to the elongated diffraction spots along the **b*** direction seen in Fig. 3(b). Note the lower resolution bright field TEM image shown in Fig. 1(b) does not reveal these stacking faults. The grain size seen in TEM is much larger than the crystallite size determined from the FWHM of XRD peak.

Other high resolution TEM images of the Nb_2O_5 film and the corresponding selected area TEM DPs were also measured from a grain with the zone axis along the [001], or **c** direction so that the [100], or **a** direction is parallel to the high resolution image. The measured unit vector length, a from the real space high resolution TEM image and TEM DP are consistent with the value of 0.6168 nm determined from the (180) peak in section 3.1.1.

3.2. Composition of Nb and O in Nb_2O_5 film

Figure 4 shows an XPS spectrum of the sample synthesized from the 5 nm thick Nb film. Six peaks including Nb $3p_{3/2}$, Nb $3p_{1/2}$, Nb $3d_{5/2}$, Nb $3d_{3/2}$, O 1s, and C 1s in the binding energy range from 150 to

550 eV are observed. The inset shows Nb $3d_{5/2}$ and Nb $3d_{3/2}$ peaks collected in a smaller energy step size from 190 to 215 eV. Quantitative composition of Nb and O near the surface can be calculated from the ratio of the Nb $3d_{5/2}$ peak area divided by the Nb sensitivity factor ($S_{Nb} = 1$) to the O 1s peak area divided by the O sensitivity factor ($S_o = 0.63$). The XPS background intensity was first subtracted from the peak area using a Shirley background subtraction and then the peak area was fitted using a Gaussian intensity distribution. The peak area and fitting error were obtained from the Gaussian fit. The peak positions for Nb $3d_{5/2}$, Nb $3d_{3/2}$, and O 1s are 207.2, 209.9 and 530.2 eV, respectively. Table 2 lists XPS peak positions measured from the Nb film and Nb_2O_5 films synthesized from the 5, 10 and 300 nm thick Nb films. Our measured binding energy of 207.2 eV from Nb $3d_{5/2}$ peak of synthesized Nb_2O_5 films is close to the binding energy 207.4 ± 1.14 eV of major oxide species reported from pure Nb_2O_5. [34] For comparison, we measured the Nb $3d_{5/2}$ peak at 202.2 eV from a pure Nb film. We observed a shift of 5.2 eV in the Nb $3d_{5/2}$ peak position for Nb_2O_5 films from that of the Nb film. This 5.2 eV shift is in agreement with the literature reported shift. [35] Our measured 202.2 eV binding energy for Nb $3d_{5/2}$ from the Nb film is close to 202.1 ± 0.79 eV recorded in the XPS handbook. The measured binding energy of 530.2 eV from O 1s peak is also close to the O 1s binding energy of 530.4 ± 1.35 eV recorded in the XPS handbook.

The O 1s and Nb $3d_{5/2}$ peak areas are 603 and 361 in arbitrary units, respectively. The ratio of O/Nb = (Area of O $1s/S_o$)/(Area of Nb $3d_{5/2}/S_{Nb}$). The calculated O to Nb ratio is 5.3/2.0. The O used in the calculated ratio of O to Nb is estimated from all detected oxygen in the surface. In addition to O that bonds to Nb, there also exists about 10 % C in the surface. This means that part of the total detected O signal may come from CO or CO_2 or H_2O near the surface. Thus our calculated ratio of O to Nb is an overestimate. We expect the actual O to Nb ratio to be less than 5.3/2.0. Similarly, the O to Nb ratio has also been obtained from films synthesized from 10 and 300 nm thick Nb films (these spectra are not

presented here). See Table 2 for the ratio of O to Nb from three film thickness. The ratios are each close to 5/2.

When the photon energy increases, it can penetrate deeper into the surface of the Nb_2O_5 film. It has been shown that energy resolved XPS with increasing photon energy (100 - 1600 eV) can reveal the nature of the suboxides. [36] Starting at 750 eV, the suboxides of Nb including NbO_2, NbO and Nb_2O (binding energy between 203 to 209 eV) exist as a transition zone between Nb_2O_5 and the Nb metal (binding energy 202.5 eV). [36] The X-ray photon energy of 1254 eV that we used can reveal the existence of the Nb suboxides in the transition zone if they exist. The fact that our XPS spectra do not reveal suboxides of Nb, but only Nb_2O_5 implies that the Nb has been fully consumed to form Nb_2O_5 and any suboxides have been converted to Nb_2O_5 after the synthesis. Therefore, there are neither detectable suboxides of Nb nor pure Nb near the surface in our sample synthesized from the 5 nm thick Nb film. Another study also supports that the outermost Nb oxide layer is always Nb_2O_5. [5] A similar XPS spectrum shows that no suboxide exists in the sample synthesized from the 10 nm thick Nb film. In contrast, for the film synthesized from the 300 thick Nb film under the same condition of 850 ^oC annealing for 30 min, there is pure Nb left near the surface. This implies that within the annealing temperature and time, the oxidation process has not consumed all the Nb in the 300 nm thick Nb film and converted it to Nb_2O_5. This is why a small (110) peak from pure Nb was observed in XRD.

3.3. Optical bandgap of Nb_2O_5 film on quartz measured from UV-Visible absorption

Figure 5(a) shows the UV-Vis reflectance and transmission spectra of the Nb_2O_5 film synthesized from the 10 nm thick Nb film on quartz. These spectra have been corrected for the quartz background measured from an annealed quartz substrate without the Nb film. A small bump exists in the reflectance spectrum around a wavelength of 300 nm. The transmittance spectrum shows a high

transmittance in the visible wavelength range, which decreases in the UV wavelength range. The resulting absorptivity coefficient, α [37] of the Nb_2O_5 film (Fig. 5(b)) shows a sharp onset around 4 eV. The optical bandgap of the Nb_2O_5 film is determined from the experimental UV-Vis absorption spectra via the Tauc method [38] by extrapolating the linear portion of the $(\alpha hv)^{½}$ vs. hv plot to the intercept, where α is the absorption coefficient, hv is the photon energy, and the exponent ½ is for an indirect bandgap. Figure 5(c) shows the Tauc analysis for the Nb_2O_5 film synthesized from the 10 nm thick Nb film on quartz which gives an optical bandgap of 3.65 ± 0.02 eV (= 340 nm).

The bandgap for bulk Nb_2O_5 is about 3.4 eV. [17] Experimentally measured bandgaps for films range from 3 to over 4 eV depending on the structural phase, grain size, and morphology of the Nb_2O_5 film as well as the exponent used in the Tauc plot. [8, 23] Our measured bandgap of 3.65 eV is close to that measured from single crystalline Nb_2O_5 nanorods grown by hydrothermal technique [18] using UV-Vis (note that the exponent of αhv used in that work was 2 instead of ½). Our value is also comparable to the value of 3.7 eV determined for pulsed laser deposited Nb film exposed in air and measured by ultraviolet photoelectron spectroscopy. [5] Density functional theory (DFT) calculations of Nb_2O_5 indicate that Nb_2O_5 is an indirect bandgap semiconductor with a bandgap of 2.55 eV. The underestimation by DFT calculations is typical due to the discontinuity of exchange correlation energy. [5]

The reflectance and transmission spectra of Nb_2O_5 film synthesized from 10 nm thick Nb film shown in Fig. 5 do not have the interference feature as compared with those of the few hundreds of nm thick Nb_2O_5 samples grown on Si substrate or glass substrates reported in previous work. [3, 6] Unlike their thicker films, our film has a much smaller dimension than the UV-Vis wavelength used in the measurement and the wave interference from the film and substrate interface does not occur.

3. 4. Film morphology and roughness

3.4.1 Atomic force microscopy

Figure 6 shows AFM images and height histograms of the 5 and 10 nm thick Nb films on SiO_2/Si(001), and the Nb_2O_5 films synthesized from the 5 and 10 nm thick Nb films on SiO_2/Si(001) substrates. The 5 and 10 nm Nb films shown in Figs. 6(a) and 6(b) are smooth and almost featureless with root mean square (RMS) roughnesses in the sub-nm range (~ 0.6 nm). In contrast, the synthesized Nb_2O_5 films shown in Figs. 6(c) and 6(d) have island-like features. The height histograms shown below the AFM images range from 0 to 25 nm with a peak around 12 nm and 0 to 30 nm with a peak around 17 nm for the Nb_2O_5 films synthesized from the 5 and 10 nm thick Nb films, respectively.

We analyzed the two-dimensional height-height correlation function, $H(\boldsymbol{r})$ from these AFM images to extract the roughness parameters including the vertical surface width, ω (or RMS roughness), lateral correlation length, ξ, and roughness exponent, α. [39-41] $H(\boldsymbol{r})$ is defined as $H(\boldsymbol{r}) = \langle [h(\boldsymbol{r}) - h(0)]^2 \rangle$, where $h(\boldsymbol{r})$ is the surface height at position $\boldsymbol{r}$ and $h(0)$ is the surface height at a reference position $\boldsymbol{r} = 0$. Surface width, ω is the square root of $\langle [h(\boldsymbol{r}) - \langle h \rangle]^2 \rangle$, where $\langle h \rangle$ is the average height of the surface. ω describes the surface roughness at large distances. The lateral correlation length, ξ describes the "wavelength" of the surface fluctuations. For large r, the surface height fluctuations should not be correlated, and $H(r) = 2\omega^2$. For small r, the surface height-height correlation has the asymptotic form $H(r) \sim r^{2\alpha}$, where α is the local roughness exponent. α describes how "wiggly" the surface is and has a value $0 < \alpha \leq 1$, with 1 being the smoothest.

To perform the height-height correlation function analysis, one needs to be aware of the sampling induced oscillation. [42] If the sampling size L is sufficiently larger than the correlation length ξ, then the oscillation will diminish when $(\xi/L)^{d/2} << 1$, where d is a dimension, and when a large number of images from a rough surface are averaged. If the oscillations do not diminish under these conditions,

then the surface is a mounded rough surface. Table 1 lists the height-height correlation function analyses of ten AFM images from each of these Nb_2O_5 films synthesized from the 5, 10 and 300 nm thick Nb films. Table 1 indicates that the vertical surface width ω increases from 3.6 ± 0.2 nm to 17.4 ± 0.3 nm, and the lateral correlation length ξ increases from 84 ± 2 nm to 193 ± 7 nm. The local roughness parameter α decreases from 0.78 to 0.61 and becomes more wiggly as the film thickness increases. The 1 × 1 μm sampling size L of the ten AFM images and the ~90 nm size of ξ, which gives $(\xi/L)^{d/2} \approx 0.09$ for $d = 2$. After averaging 10 images, the height-height correlation function still has obvious oscillations with regular separation. This is consistent with results obtained for a rough surface with mounds. [42] These mounds are seen as islands in the AFM images shown in Figs. 6(c) and 6(d).

From Table 1, the lateral correlation length ξ extracted from AFM is larger than the average grain size obtained from GIXRD. This implies that there is more than one grain in each morphological feature. For the Nb_2O_5 film synthesized from the 300 nm thick Nb film, the value of ξ is of the same order of magnitude as the lateral size obtained from the TEM cross section view shown in Fig. 1(b).

3.4.2 X-ray specular reflectivity

X-ray specular reflectivity (XRR) curves were obtained to probe the thickness, roughness, and density of the niobium oxide film on quartz. X-rays are incident at a grazing angle and reflect off from various interfaces of a thin film resulting in an interference pattern as the angle of incidence changes. Figure 7 shows the XRR curve vs. momentum transfer, q ($Å^{-1}$) resulting from the Nb_2O_5 film synthesized from the 10 nm Nb film on a quartz substrate following an annealing at 850 °C. The dependence of the oscillatory reflectivity observed in the interference pattern, or Kiessig fringes, on thickness can be described by the Bragg equation. A more detailed description can be found elsewhere. [43, 44] The XRR profile was modeled as a thin Nb_2O_5 film on top of a SiO_2 substrate using the LEPTOS software suite

from Bruker AXS. The model was fitted to the data using the thickness of the niobium oxide film, and the roughness and density of both the film and substrate as variables.

The Nb_2O_5 film thickness was determined to be 22.57 ± 0.09 nm with a surface roughness of 2.2 ± 0.3 nm from the XRR curve. This thickness is higher than the histogram shown in Fig. 6(b) probably due to the AFM tip size effect when imaging the depth of closely spaced small features. The density was determined to be 5.34 ± 0.07 g/cm^3, which agrees, approximately, with the orthorhombic density of 5.24 g/cm^3 [32] and is slightly higher than the TT and T phases of Nb_2O_5, of 4.99 and 5.00 g/cm^3, respectively. [45] Using the density of the 10 nm Nb film thickness, and considering the stoichiometric ratio in mass change by converting Nb to Nb_2O_5 (2 Nb + 2.5 O_2 → Nb_2O_5), we can estimate the expected density of the 22 nm thick Nb_2O_5 film to be 5.43 g/cm^3.

3. 5. Vibrational modes of Nb_2O_5 films from Raman spectra

Figure 8 shows three Raman spectra: (a) the reference spectrum of a bare SiO_2 covered Si(001) substrate after 850 ^{o}C annealing for 30 min; (b) the spectrum of the Nb_2O_5 film synthesized from the 5 nm thick Nb film; (c) the difference between the Nb_2O_5 film synthesized from the 5 nm thick Nb film and the reference spectrum. The reference spectrum in Fig. 8(a) shows two Si peaks, a sharp peak around 521 cm^{-1} and a broad peak around 972 cm^{-1}. Both Si peaks also show up with high intensity in the Raman spectrum of the Nb_2O_5 film shown in Fig. 8(b). For the 532 nm laser wavelength that we used in our experiment, the optical penetration depth is about 0.7 μm and the photon energy is 2.33 eV, which is higher than the Si bandgap of 1.11 eV. Raman resonances [46] occur at 521 cm^{-1} and 972 cm^{-1} as shown in Fig. 8(a). In order to remove the observed enhancement effect in Raman intensity from the Si(001) substrate when a 532 nm incident laser wavelength is used, we subtracted the reference

spectrum shown in Fig. 8(a) from the spectrum shown in Fig. 8(b). The difference spectrum shown in Fig. 8(c) has five distinct Raman peaks at 238, 304, 647, 695, and 993 cm^{-1}.

Among the five peaks, the full-width-at-half-maximum (FWHM) of the Raman peaks in the difference spectrum Fig. 8(c) varies from sharp to broad. The broad peak may contain more than one peak. Using Origin peak fit software we have fitted the broad peaks and obtained extra peaks with the coefficient of determination (goodness of fit) = 0.992. The positions of peaks in the Raman difference spectra from our Nb_2O_5 films synthesized from the 5, 10, and 300 nm Nb films are listed in columns 3, 4 and 5 in Table 3. For a comparison, Nb_2O_5 powder samples [47] and Nb_2O_5 nanowires [10] are also listed in the last column in the same table. Note that the phase of Nb_2O_5 in these works is monoclinic (a = 2.13 Å, b = 3.81 Å, and c = 1.95 Å) and not orthorhombic. The laser wavelength used in Raman scattering is 514.5 nm. [47] The symbols S, M, and W in the last column correspond to strong, medium and weak Raman peaks, respectively. It is seen from Table 3 that all strong peaks observed in the Nb_2O_5 powders are observed in our Nb_2O_5 films, but that the same is not true for the weak peaks. Some of our peak positions do not match exactly those of the Nb_2O_5 powders. This may be due to the fact that our Nb_2O_5 film is an orthorhombic phase. Also, it is on the SiO_2 surface and the film-substrate interaction may change the vibrational modes of the Nb_2O_5 film. For a powder sample, if the powder thickness is larger than the penetration depth of the laser, the substrate has no effect on the Raman spectrum. Theoretical modeling is needed to understand the observed difference in Raman shifts shown in Table 3.

Table 3 lists the vibrational modes and their ranges of Raman shifts in columns 1 and 2, respectively. In the 700 - 1000 cm^{-1} range, the Raman peak around 993 cm^{-1} is a longitudinal optical (LO), A_{1g} mode using Mulliken symbols. [11, 48] This vibration is most prominent in oxide systems. It is a symmetric single stretching vibration mode (symbol A) of Nb and O double bond (Nb=O) relative to the principle rotational axis (symbol 1) and an inversion through the center of the molecule (symbol g). This

stretching mode has a short bond and is also supported by the DFT calculation result described previously. [49] This peak is also sensitive to ordering. The peak intensity is either low or zero if the structure is disordered. [48] The FWHM of this peak is ~ 20 cm^{-1}, which is relatively narrow, implying a reasonably ordered film. In the 700 - 1000 cm^{-1} range there are two other peaks at 962 and 722 cm^{-1}. These are single Nb and O (Nb-O) stretching bonds associated with NbO_6 and NbO_4. In the range of 600 - 700 cm^{-1} we observed three transverse optical (TO), E_g (Symbol E is doubly degenerated modes) modes. In the range of 200 - 300 cm^{-1} we observed $T_{2\mu}$ modes (T is triply degenerated modes, 2 and μ are anti-symmetric to a rotation axis and an inversion, respectively). However, for the Nb_2O_5 films synthesized from 5 and 10 nm thick Nb films, we did not observed T_{2g} modes in the range of 350 - 550 cm^{-1}.

4. Discussions

4. 1. Formation of Nb_2O_5 films in Ar flow

Previous ultraviolet photoemission spectroscopy studies of oxygen adsorption on Nb(110) surface at 300 K in ultrahigh vacuum showed that oxygen molecules dissociated and chemisorbed on the Nb(110) surface. NbO and NbO_2 formed initially as protective layers and then Nb_2O_5 formed after heavy oxidation. [50] In our case, the sputtered Nb films deposited on SiO_2/Si(001) were heated up to 850 ^oC (1123 K) in a furnace and the oxygen came from the exogenous oxygen in the SiO_2 and as impurity in the Ar flow. Based on the heat of formation of Nb_2O_5 as compared to that of SiO_2, Nb is not an effective reductant towards SiO_2. [51] When Nb was deposited on the SiO_2 surface, the high heat of formation of Nb_2O_5 (-1899.54 kJ/mol) was higher than that of SiO_2 (-879.48± 2.93 kJ/mol). Assume the following reaction: $4\ Nb + 5\ SiO_2 \rightarrow 2\ Nb_2O_5 + 5\ Si$. Then $\Delta H_{reaction}$ = 2 (-1899.54 kJ/mol) - 5 (-879.48 kJ/mol) = + 598.32 kJ/mol. The positive heat of reaction means this reaction is endothermic and therefore the reduction of SiO_2 cannot be the origin of oxygen for the formation of the Nb_2O_5 films. The TEM cross section shows that the thickness of SiO_2 is about 300 nm. The oxygen must come from

external sources such as impurities in the Ar gas supply. During our synthesis of Nb_2O_5, there was no external oxygen flow or oxygen plasma. The fact that Nb_2O_5 was formed after 850 ^oC annealing for 30 min under Ar flow in a furnace implies there were oxygen supplies in the Ar flow. One of the major oxygen containing chemicals in the air is the oxygen molecule. Its density is about 21 % of air density (2.504×10^{19} atoms/cm^3) or 5.24×10^{18} atoms /cm^3 under 1 ATM at 20 ^oC. Other minor oxygen containing chemicals are water molecules (1-5 %) and CO_2 molecules (0.03 %). All these oxygen containing molecules are available for oxidation reaction. The Ar flow reduces the amount of air flow and therefore the oxygen supply from the air is reduced. In an ultrahigh vacuum environment, the Nb_2O_5 film can only grow to a thickness of ≤ 2 nm in an ultrahigh vacuum furnace at 1850 ^oC for 2 hours because of the much reduced amounts of oxygen and water. [35] We have also synthesized a Nb_2O_5 film from the 10 nm Nb film in air without Ar flow. The XRD of this sample shows many additional peaks (not shown here). In contrast, the sample prepared under Ar flow shows only the (001) and (002) XRD peaks (see Fig. 2).

The growth of Nb oxides in the presence of O_2, H_2O and H_2O_2 is described by Cabrera Mott theory. [52] Once the initial Nb oxide is formed, the anion (O^-) diffusion in the oxide film is significant compared with cation (Nb^+) diffusion and the new oxide layers are initiated at the oxide-metal interface. The oxidation steps are $Nb \rightarrow NbO \rightarrow NbO + NbO_2 \rightarrow Nb_2O_5$. The oxygen reacted with the Nb film to form Nb_2O_5 at the interface between Nb and oxygen in the Ar flow ambient. After all the Nb atoms at or near the interface were consumed, the oxygen reacted with Nb atoms located further away from the interface. The formation of Nb_2O_5 was supported by our XRD, TEM and XPS results described above.

4. 2. Dominant [001] growth orientation in Nb_2O_5 films

Recent *ab initio* density functional theory calculation (DFT) of monolayer oxygen adsorption on Nb(110) using linear augmented plane wave method (LAPW) indicates that oxygen atoms form

stronger bonds with Nb atoms on the (110) surface in the [001] direction rather in the $[1\bar{1}0]$ direction. The stronger bond shortens the bond length between Nb and O in the [001] direction. The shorter bond results in a structural relaxation in neighboring Nb atoms. [49] This DFT result qualitatively agrees with our XRD finding that the oxygen reacts with (110) surface of Nb and that the dominant oxide orientation is the [001] direction. Previous work shows that the unit cell of the orthorhombic Nb_2O_5 has 16.8 Nb ions and 42 oxygen atoms. [32] Eight Nb ions are in distorted octahedral positions, and eight Nb ions are in pentagonal bipyramid positions. Both groups are in a sheet parallel to the (001) plane. These 16 Nb ions are surrounded by six or seven oxygen atoms. The remaining 0.8 Nb ion is positioned at the interstitial nine-coordinated site in the unit cell. [53] The adjacent spacing among Nb atoms is not uniform in the [010] or **b** direction. This is consistent with the high resolution TEM image along the **b** direction shown in Fig. 3(a).

5. Summary

We report the annealing of Nb films grown on amorphous substrates and show that optically smooth orthorhombic Nb_2O_5 films can be formed at 850 ^oC in a short time under Ar flow in a furnace. This takes advantage of the high heat of formation of Nb_2O_5. The oxide film thickness is two to three times thicker than that of the starting Nb film as shown by TEM and X-ray reflectivity measurements. Therefore the thickness of Nb_2O_5 film can be controlled by altering the starting Nb film thickness. The composition ratio of Nb/O determined by XPS is close to 2/5. The optical bandgap is ~ 3.65 eV. The low optical transmittance in the UV wavelength range and high transmittance in the visible wavelength range indicate potential applications in UV detection, photocatalysis and electrochromic devices. Although we have not measured the mechanical properties of our synthesized Nb_2O_5 films, other work shows the Nb_2O_5 films is scratch resistance and hydrophobic. [3] Our simple growth method can be scaled up and can have potential realistic applications.

Acknowledgement

This work is supported by New York State Foundation of Science, Technology and Innovation (NYSTAR) through Focus Center-New York, and Rensselaer. TEM study was carried out in whole at the Center for Functional Nanomaterials, Brookhaven National Laboratory, which is operated by the U.S. department of Energy, Office of Basic Sciences, under contract no. DE-AC02-98CH10886. PHD acknowledges support from the National Science Foundation CHE-1255100. We thank A. Littlejohn for editing the manuscript.

Notes and References:

[a] Department of Physics, Applied Physics and Astronomy, Rensselaer Polytechnic Institute, 110 8th Street, Troy, New York 12180, USA

[b] Department of Chemistry and Chemical Biology, Rensselaer Polytechnic Institute, 110 8th Street, Troy, New York 12180, USA

[c] Brookhaven National Lab, Center for Functional Nanomaterials Bldg. 735, P.O. Box 5000, Upton, New York 11973

* Corresponding Author: jatiskumar@gmail.com , dashj@rpi.edu

1 O. Kubaschewski and E. L. Evans, *Metallurgical thermochemistry*, Pergamon Press, NY, 1958.

2 D. Rosenfeld, R. Sanjines, F. Levy, P. Buffat, V. Demarne and A. Grisel, *Journal of Vacuum Science & Technology A*, 1994, **12**, 135-139.

3 M. Mazur, M. Szymanska, D. Kaczmarek, M. Kalisz, D. Wojcieszak, J. Domaradzki and F. Placido, *Applied Surface Science*, 2014, **301**, 63-69.

4 A. Pignolet, G. M. Rao and S. Krupanidhi, *Thin solid films*, 1995, **261**, 18-24.

5 Z. Weibin, W. Weidong, W. Xueming, C. Xinlu, Y. Dawei, S. Changle, P. Liping, W. Yuying and B. Li, *Surface and Interface Analysis*, 2013, **45**, 1206-1210.

6 O. D. Coskun and S. Demirela, *Applied Surface Science*, 2013, **277**, 35-39.

7 T. Blanquart, J. Niinisto, M. Heikkila, T. Sajavaara, K. Kukli, E. Puukilainen, C. Xu, W. Hunks, M. Ritala and M. Leskela, *Chemistry of materials*, 2012, **24**, 975-980.

8 G. Agarwal and G. Reddy, *Journal of Materials Science: Materials in Electronics*, 2005, **16**, 21-24.

9 F. Lenzmann, V. Shklover, K. Brooks and M. Gratzel, *Journal of Sol-Gel Science and Technology*, 2000, **19**, 175-180.

10 M. Mozetic, U. Cvelbar, M. K. Sunkara and S. Vaddiraju, *Advanced Materials*, 2005, **17**, 2138-2142.

11 B. Varghese, S. C. Haur and C.-T. Lim, *The Journal of Physical Chemistry C*, 2008, **112**, 10008-10012.

12 Z. Wang, Y. Hu, W. Wang, X. Zhang, B. Wang, H. Tian, Y. Wang, J. Guan and H. Gu, *international journal of hydrogen energy*, 2012, **37**, 4526-4532.

13 P. George, V. Pol and A. Gedanken, *Nanoscale Research Letters*, 2007, **2**, 17-23.

14 W. Hu, Y. Mi, D. Tian, Y. Zhao, Z. Liu, K. Yao and Y. Zhu, *Materials Chemistry and Physics*, 2008, **109**, 184–188.

15 H. Luo, M. Wei and K. Wei, *Journal of Nanomaterials*, 2009, **2009**, 35, 1- 4.

16 Y. Kobayashi, H. Hata, M. Salama and T. E. Mallouk, *Nano letters*, 2007, **7**, 2142-2145.

17 C. Yan and D. Xue, *Advanced Materials*, 2008, **20**, 1055-1058.

18 J. Liu, D. Xue and K. Li, *Nanoscale research letters*, 2011, **6**, 138, 1-8.

19 X. Fang, L. Hu, K. Huo, B. Gao, L. Zhao, M. Liao, P. K. Chu, Y. Bando and D. Golberg, *Advanced Functional Materia*ls, 2011, **21**, 3907-3915.

20 V. Galstyan, E. Comini, G. Faglia and G. Sberveglieri, *CrystEngComm*, 2014, **16**, 10273-10279.

21 R. Abdul Rani, A. Zoolfakar, J. Ou, M. Field, M. Austin and K. Kalantar Zadeh, *Sensors and Actuators B: Chemical*, 2013, **176**, 149-156.

22 T. Athar, A. Hashmi, A. Al-Hajry, Z. Ansari and S. Ansari, *Journal of nanoscience and nanotechnology*, 2012, **12**, 7922-7926.

23 R. Shao, Z. Cao, Y. Xiao, H. Dong, W. He, Y. Gao and J. Liu, *RSC Advances*, 2014, **4**, 26447.

24 Y. Zhao, X. Zhou, L. Ye and S. C. E. Tsang, *Nano Reviews*, 2012, **3,** 1-11.

25 D. R. Rosseinsky and R. J. Mortimer, *Advanced Materials*, 2001, **13**, 783-793.

26 S. Choi, J. Wang, Z. Cheng and M. Liu, *Journal of The Electrochemical Society*, 2008, **155**, B449-B454.

27 C. C. Chusuei and D. W. Goodman, *Encyclopedia of Physical Science and Technology*, 2002, **17**, 921-938.

28 G. Harp, D. Saldin and B. Tonner, *Journal of Physics: Condensed Matter*, 1993, **5**, 5377-5388

29 B. E. Warren, *Journal of the American Ceramic Society*, 1992, **75**, 5-10.

30 L. Chen, P. Shimpi, T.-M. Lu and G.-C. Wang, *Materials Chemistry and Physics*, 2014, **145**, 288-296.

31 S. Mahieu, P. Ghekiere, D. Depla and R. De Gryse, *Thin solid films*, 2006, **515**, 1229-1249.

32 K. Kato and S. Tamura, *Acta Crystallographica Section B: Structural Crystallography and Crystal Chemistry*, 1975, **31**, 673-677.

33 C. A. Schneider,W. S. Rasband and K.W. Eliceiri, *Nature methods*, 2012, **9**, 671-675.

34 B. V. Crist, *Handbook of monochromatic XPS spectra*, XPS International, 1999.

35 M. Grundner and J. Halbritter, *Journal of Applied Physics*, 1980, **51**, 397-405.

36 H. Tian, *Surface Oxide Study On Solid Niobium For Superconducting RF Accelerators Using Variable Photon Energy XPS*, SRF Workshop, 2007.

37 E. D. Palik, *Handbook of optical constants of solids*, Academic press, 1998, vol. 3.

38 J. Tauc, R. Grigorovici and A. Vancu, *physica status solidi (b)*, 1966, **15**, 627-637.

39 S. Sinha, E. Sirota, S. Garoff and H. Stanley, *Physical Review B*, 1988, **38**, 2297-2312.

40 A. Barabasi and H. Stanley, *Fractal concepts in surface growth*, Cambridge University Press, Cambridge, 1995

41 Y.-P. Zhao, G.-C. Wang and T.-M. Lu, *Characterization of amorphous and crystalline rough surface: principles and applications*, Academic Press, (Experimental Methods in the Physical Science Vol. 37), 6th edn, 2001.

42 H.-N. Yang, Y.-P. Zhao, A. Chan, T.-M. Lu and G.-C. Wang, *Physical Review B*, 1997, **56**, 4224-4232

43 E. Chason and T. Mayer, *Critical Reviews in Solid State and Material Sciences*, 1997, **22**, 1-67.

44 G. Evmenenko, M. Van der Boom, J. Kmetko, S. Dugan, T. Marks and P. Dutta, *The Journal of Chemical Physics*, 2001, **115**, 6722-6727.

45 M. A. Aegerter, *Solar energy materials and solar cells*, 2001, **68**, 401-422.

46 J. Kreisel, M. C. Weber, N. Dix, F. Sanchez, P. A. Thomas and J. Fontcuberta, *Advanced Functional Materials*, 2012, **22**, 5044-5049.

47 U. Balachandran and M. Eror, *Journal of Mater. Sci. Lett*, 1982, **1**, 374-376.

48 A. McConnell, J. Aderson and C. Rao, *Spectrochimica Acta Part A: Molecular Spectroscopy*, 1976, **32**, 1067-1076.

49 D. Kilimis and C. E. Lekka, *Materials Science and Engineering: B*, 2007, **144**, 27-31.

50 R. Franchy, T. Bartke and P. Gassmann, *Surface science*, 1996, **366**, 60-70.

51 J. Cox, D. Wagman and V. Medvedev, *Key Values for Thermodynamics*; Hemisphere Publishing Corp.: New York, 1989.

52 N. Cabrera and N. Mott, *Reports on progress in physics*, 1949, **12**, 163-184.

53 J. W. Kim, *Synthesis and characterization of nanostructured transition metal oxides for energy Storage devices*, UCLA Electronic Thesis and Dissertations, http://escholarship.org/uc/item/34z248mr, 2012.

Figure captions:

Fig. 1 (a) Schematic of sputtered Nb film on 300 nm thick amorphous SiO_2 on 500 μm thick Si(001) substrate. The schematic is not to scale. (b) TEM cross section image of a synthesized $Nb_2O_5/SiO_2/Si(001)$ sample from 300 nm thick Nb film on $SiO_2/Si(001)$ after 850 ^oC annealing for 30 min.

Fig. 2 Grazing incidence X-ray diffraction (GIXRD) *vs.* two theta scans from amorphous $SiO_2/Si(001)$, sputtered 5 nm $Nb/SiO_2/Si(001)$ at room temperature, and synthesized $Nb_2O_5/SiO_2/$ Si(001) from 5, 10, 100, and 300 nm thick Nb annealed at 850 ^oC for 30 min. The grazing incident angle is fixed at 1.5^o from the surface.

Fig. 3 (a) High resolution real space TEM image (scale bar is 2 nm) and (b) TEM diffraction pattern (scale bar is 1 nm^{-1}) of Nb_2O_5 film synthesized from 300 nm thick Nb grown on 300 nm thick $SiO_2/Si(001)$ and annealed at 850 ^oC for 30 min.

Fig. 4 X-ray photoelectron spectroscopy survey spectrum of $Nb_2O_5/SiO_2/Si(001)$ synthesized from 5 nm thick Nb film on $SiO_2/Si(001)$. The inset shows the spectrum of Nb $3d_{5/2}$ and Nb $3d_{3/2}$ peaks using finer binding energy step size during data collection. The O 1s and Nb $3d_{5/2}$ peak areas were used to estimate the ratio of atomic percentage of oxygen to atomic percentage of Nb near surface. The ratio is about 5.3 to 2.0.

Fig. 5 (a) UV-Vis reflectance (solid blue curve) and transmission (dashed red curve) *vs.* wavelength spectra of Nb_2O_5 film synthesized from 10 nm thick Nb on quartz substrate annealed at 850 ^oC for 30 min. (b) Calculated absorptivity coefficient from the reflectance and transmission data. (c) Tauc plot of the absorptivity coefficient for the Nb_2O_5 film.

Fig. 6 Atomic force microscopy images (5 μm × 5 μm) and histograms of (a) 5 nm thick Nb film and (b) 10 nm thick Nb film on SiO_2/Si(001) before synthesis. AFM images (1 μm × 1 μm) of Nb_2O_5/SiO_2/Si(001) synthesized from (c) 5 nm thick Nb film and (d) 10 nm thick Nb film.

Fig. 7 X-ray specular reflectivity curve (black filled circles) and fitted model (red curve) *vs.* momentum transfer **q** for the Nb_2O_5 film synthesized from 10 nm thick Nb film on quartz substrate.

Fig. 8 Raman shift spectra measured at room temperature. (a) SiO_2/Si(001) that was annealed at 850 ^oC for 30 min and cooled down to room temperature, (b) Nb_2O_5/SiO_2/Si(001) synthesized from 5 nm thick Nb film, (c) Difference spectrum of (b) minus (a) to remove Si substrate contribution. Peak fit of difference spectrum of Nb_2O_5/SiO_2/Si(001) synthesized from 5 nm thick Nb film in three Raman shift regimes (d) 100-500 cm^{-1}, (e) 500-800 cm^{-1}, and (f) 800-1100 cm^{-1}.

Table 1: Bragg peak and average ordered crystallite size from XRD and film's roughness parameters including surface width, correlation length and roughness exponent from AFM

Sample (nm)		GIXRD		AFM		
		Orientation (XRD Bragg peak)	Ave. ordered crystalline size (nm)	Surface width ω (nm)	Correlation length ξ (nm)	Roughness exponent α
5 nm Nb		110 (38.6°)	5.5 ± 0.1	----	----	----
Nb_2O_5 Synthe-sized films from	5 nm Nb	001 (22.6°), 002 (46.1°)	12.5 ± 0.2	3.6 ± 0.2	84 ± 2	0.78
	10 nm Nb	001(22.6°), 002 (46.1°)	18.6 ± 0.4	3.8 ± 0.2	91 ± 2	0.72
	300 nm Nb	001 (22.6°), 002 (46.1°) 180 (28.4°), 181(36.6°), 380(50.9°), 182(55.1°)	42.6 ± 0.4	17.4 ± 0.3	193 ± 7	0.61

Table 2: Measured binding energies of Nb in Nb film and Nb in Nb_2O_5 films from XPS. The "----" means no peak.

Samples		Binding energy of Nb in Nb film (eV)		Binding energy of major species in Nb_2O_5 films (eV)						Ratio of O to Nb
		Nb $3d_{5/2}$	Nb $3d_{3/2}$	Nb $3d_{5/2}$	Nb $3d_{3/2}$	C 1s	Nb $3p_{3/2}$	Nb $3p_{1/2}$	O 1s	
	5 nm Nb	202.2	205.0	----	----	285	----	----	530.1	
Nb_2O_5 synthe-sized from	5 nm Nb	----	----	207.2	209.9	285	365.4	381.2	530.2	5.30/2
	10 nm Nb	----	----	207.2	209.9	285	365.4	381.2	530.2	5.31/2
	300 nm Nb	----	204.9	207.2	209.9	285	365.4	381.2	530.2	5.34/2

Table 3 Raman peaks of Nb_2O_5 films synthesized from 5, 10, and 300 nm thick Nb films and their comparison with Nb_2O_5 powders and nanowires.

Vibrational mode	Raman shift range (cm^{-1})	Raman shift of film synthesized from			Monoclinic Nb_2O_5 powders, [47] Nanowires on Ni foil in oxygen plasma [10]
		5 nm Nb	10 nm Nb	300 nm Nb	
$T_{2\mu}$	200 - 300	217.65	217.63	220.58	207 (M)
		238.70	238.71	238.71	235 (S)
					261 (S)
		304.29	304.25	268.81	305 (M)
		311.96	312.14	301.51	
		324.23	324.22	359.27	
T_{2g}	350 - 560			470.51	347 (W)
					471 (W)
					550 (W)
TO mode E_g	600 - 700				632 (S)
		647.65	647.65	647.24	647 (S)
		666.88	666.85	682.63	659 (S)
		695.72	695.75		674 (S)
LO mode A_{1g}	700 - 1000	722.79	725.23	707.47	760 (W)
				752.70	
					846 (W)
					897 (W)
				896.12	
		962.65	962.68	962.21	
		992.62	993.54	993.84	992 (S)

FIG 1:

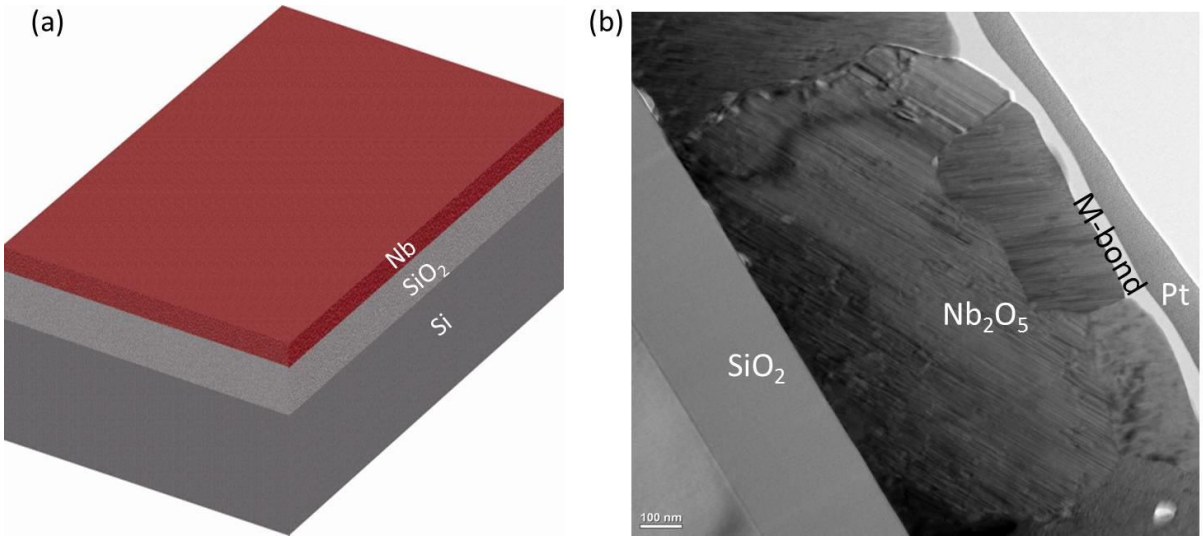

FIG 2:

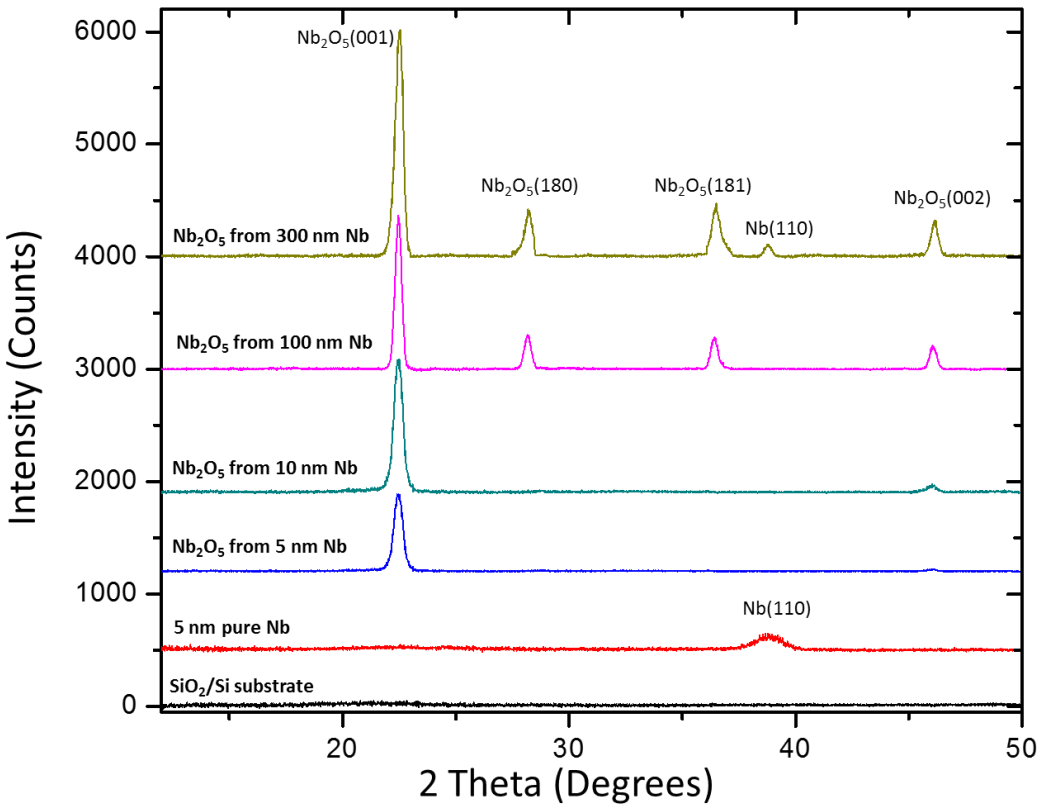

FIG 3:

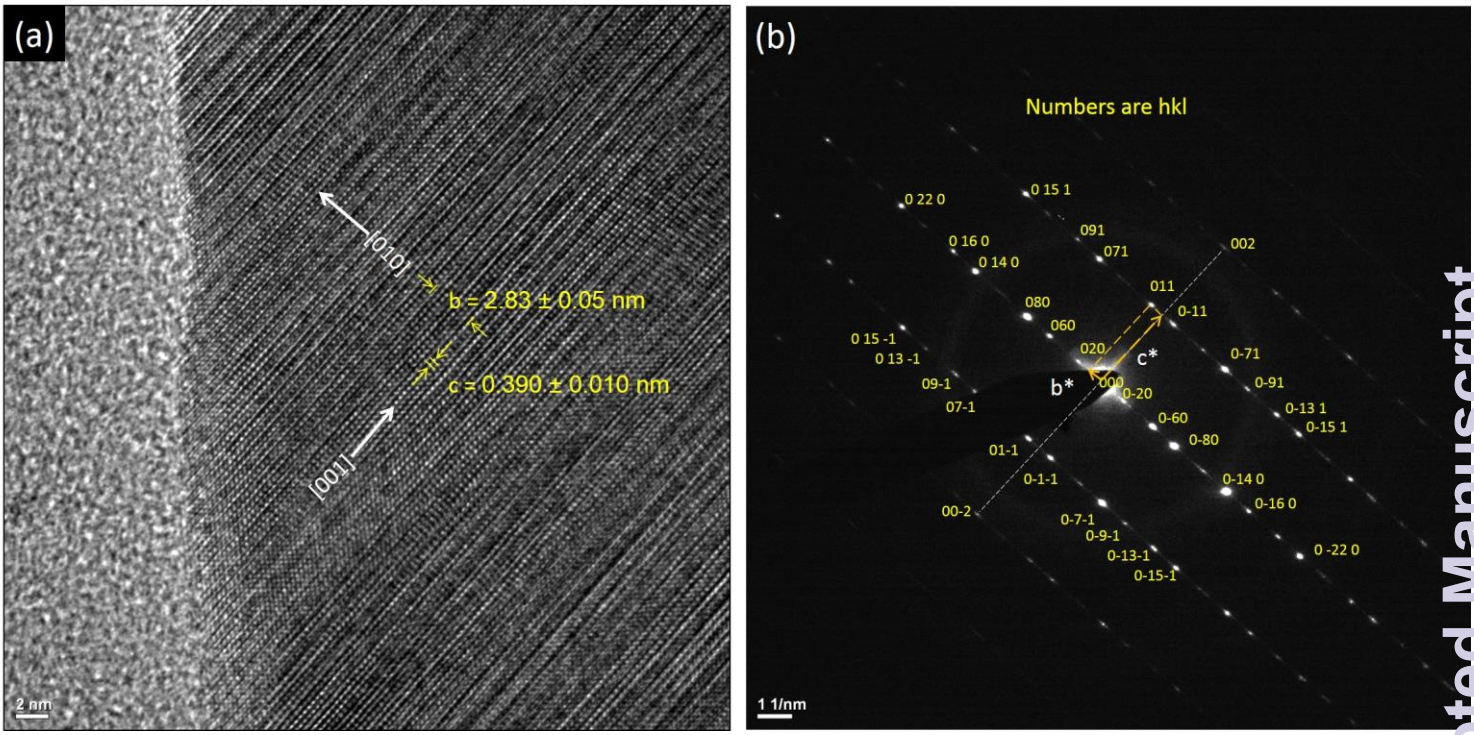

FIG 4:

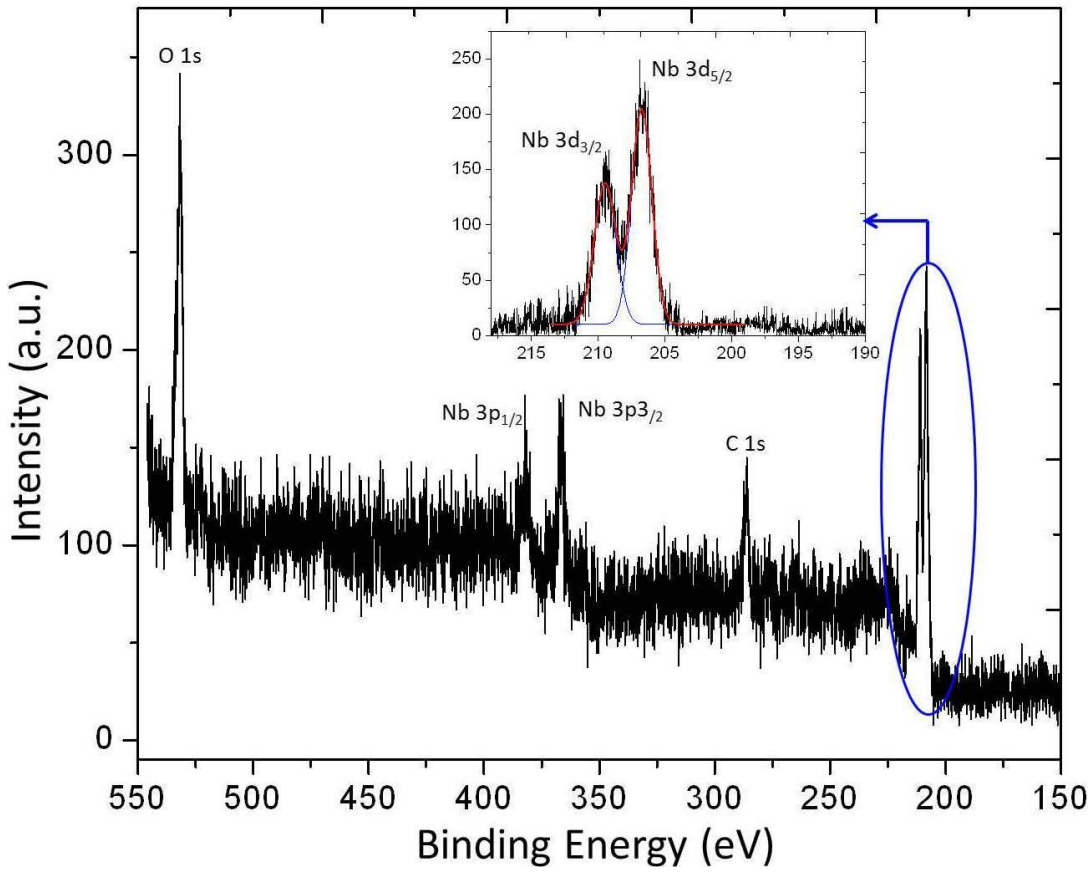

FIG 5:

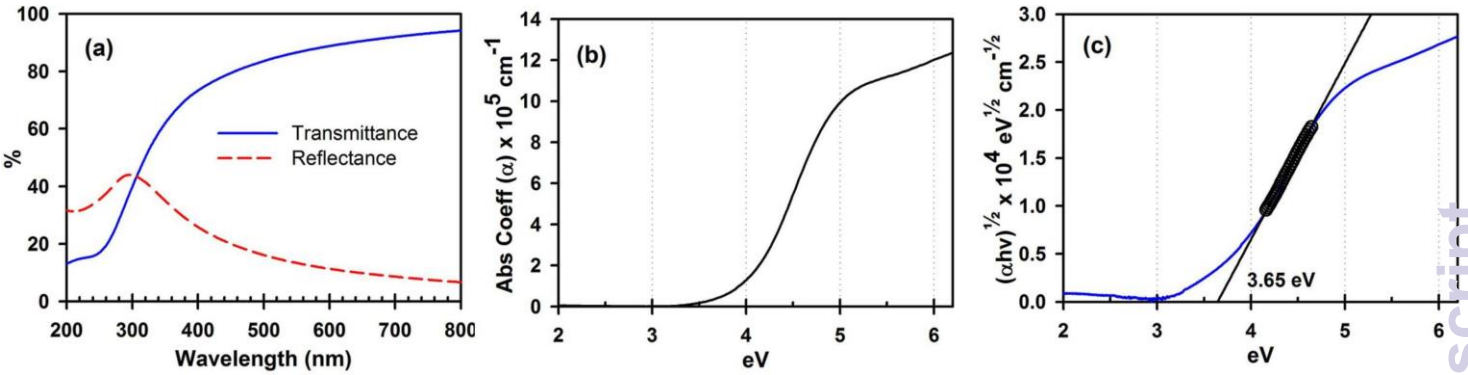

FIG 6 :

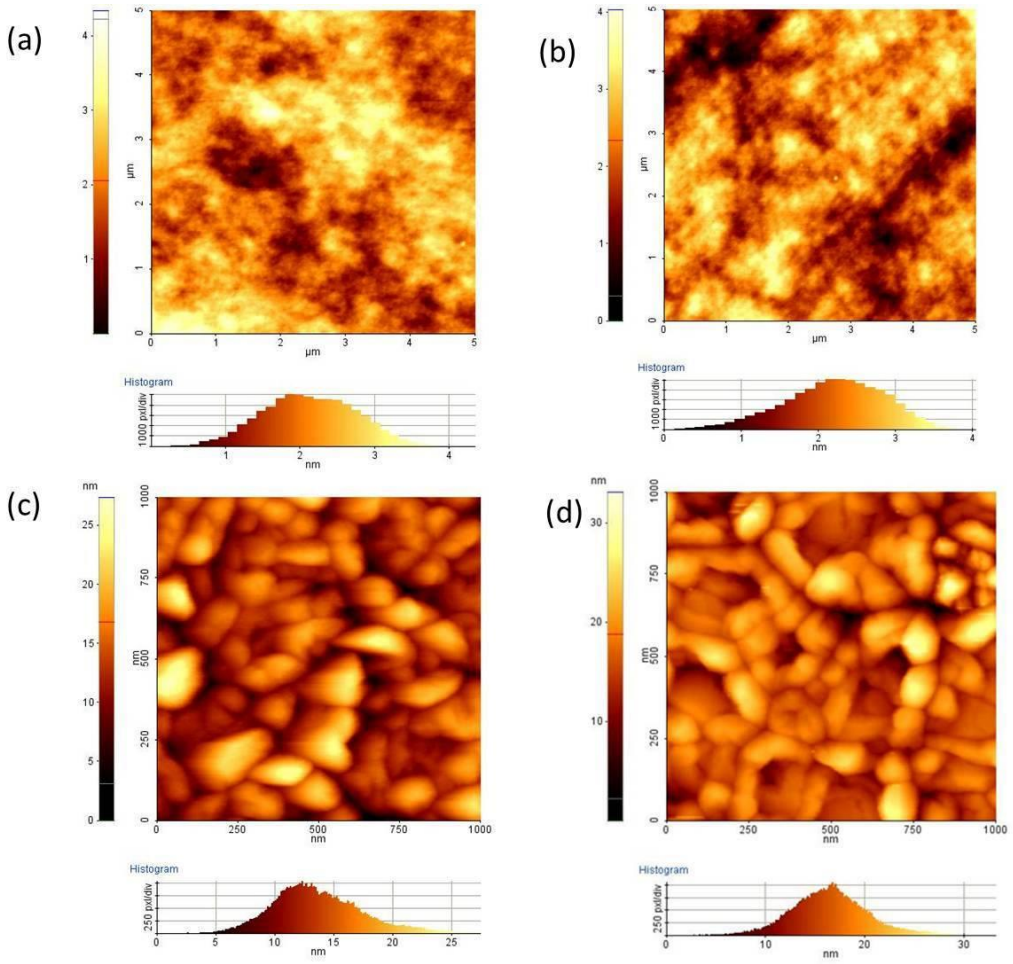

FIG 7:

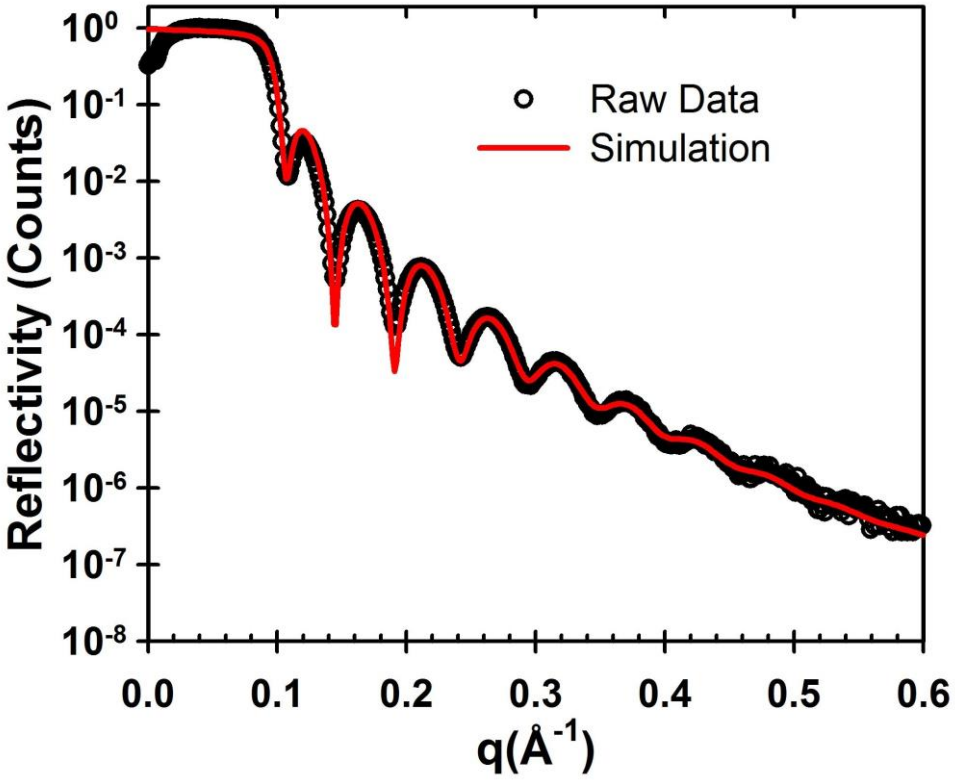

FIG 8: